Korean J. Chem. Eng., 40(8), 1901-1911 (2023)
DOI: 10.1007/s11814-023-1486-z

pISSN: 0256-1115
eISSN: 1975-7220

Electrospun PVDF-HFP/PAN bicomponent nanofibers as separators in lithium-ion batteries with high thermal stability and electrolyte wettability

Jaeseon Lee*,, Jinsoo Yoon*, Jaesung Jeon***, Yohan Hong****, Seong-Geun Oh*,†, and Hoon Huh**,†**

*Department of Chemical Engineering, Hanyang University, Seoul 04763, Korea
**Carbon Neutral Technology R&D Department, Korea Institute of Industrial Technology, Cheonan, Chungnam 31056, Korea
***Department of Materials Science and Engineering, Inha University, Incheon 22212, Korea
****Grapsil, Korea Institute of Industrial Technology, Cheonan, Chungnam 31056, Korea
(*Received 20 November 2022 • Revised 11 March 2023 • Accepted 1 May 2023*)

Abstract−Battery reliability is emerging as a new challenge due to the thermal stability and electrolyte wettability of polyolefin separators used in lithium-ion batteries. In this study, a method to improve the thermal stability and electrolyte wettability of a polyolefin separator is proposed. Bicomponent nanofibers were successfully fabricated by electrospinning poly (vinylidene fluoride-co-hexafluoropropylene) (PVDF-HFP) with high ionic conductivity and polyacrylonitrile (PAN) with excellent thermal stability. The nanofiber-based separator of PVDF-HFP/PAN exhibited high porosity (60-76%), electrolyte uptake (≅2,000%), and thermal stability (5%<shrinkage, at 200 °C) than conventional polyolefin separator. The battery using the bicomponent nanofiber separator composed of PVDF-HFP and PAN showed better cycle performance (421 mAh/g, after 80 cycle), efficiency (≅99.6%), and c-rate performance (418 mAh/g, 3C) than the battery using polyolefin separator.

Keywords: Electrospinning, Bicomponent Nanofiber, PVDF-HFP/PAN, Thermal Stability, Electrolyte Wettability, Separator

INTRODUCTION

As the demand for energy storage systems and equipment increases, rechargeable secondary batteries are attracting considerable attention [1-5]. Secondary batteries come in the form of lead-acid accumulators (lead storage batteries), nickel-cadmium batteries, nickel-metal-hydride batteries, a lithium-ion battery (LIB), a redox flow battery, and an N-S battery. Among these, LIBs are widely used in electrical devices and vehicles due to their high specific energy, efficiency, long life, and low memory effect [6]. Since the advent of practical LIBs, researchers have attempted to replace each battery component with a new type of material to improve energy and power density, electrochemical stability, and cycle performance [7-9]. As one of the main components of LIB, a separator physically separates the cathode and the anode to prevent electrical shorts and serves as a passageway for ions [10,11]. A separator is a major component responsible for battery safety as battery cycle performance and stability increase with ion mobility.

Commercially available LIB separators use a polyolefin-based polyethylene (PE) and polypropylene (PP) polymer. Among polyolefin-based polymers, PE is the most common choice for battery separators because it is inexpensive, chemically stable, and mechanically robust [12]. However, because polyolefin-based PE separators are not polar, the electrolyte, which is a polar solvent, is not sufficiently absorbed, leading to low ion conductivity and poor battery cycle performance. In addition, the high crystallinity of PE reduces ion mobility and causes an electrical short inside the battery due to high separator shrinkage at high-temperature environments [13]. Despite the many advantages of polyolefin-based separators, LIB separators need to be replaced due to the disadvantages created by poor electrochemical stability [13]. As a product to replace a polyolefin separator, a nonwoven separator has recently received industrial attention as a possible LIB separator. Nonwoven membranes can replace polyolefin PE membranes because they can have a great deal of electrolyte wettability due to their high porosity and specific surface area [14-16]. Various methods exist to prepare uniform nanosized fibers. Among them, electrospinning technology is attracting attention in the manufacture of non-woven fabric separators for LIB because it can easily and inexpensively manufacture nanofibers. A polymer-based nanofiber separator was found to improve ionic conductivity, electrochemical performance, and battery stability compared with a polyolefin separator [17]. Various electrospinning methods are available for fabricating a nonwoven separator, including co-electrospinning [18], blend spinning [19], layer-by-layer spinning [20,21], axial spinning [22,23], and side-by-side spinning [24]. Among them, blend spinning is a simple, convenient, and cost-effective method of producing a nonwoven fabric with excellent material performance [19]. Poly(vinylidene fluoride) (PVDF) [26, 27], poly(vinylidene fluoride-co-hexafluoropropylene) (PVDF-HFP) [28,29], polyacrylonitrile (PAN) [28,30,40], polyimide [31-33], polyethylene terephthalate (PET) [33,34], polyvinyl chloride (PVC) [35, 36], poly(methyl methacrylate) (PMMA) [37,38], and polystyrene (PS) [39] nonwoven fabric membranes have been tested as separators that can reduce thermal shrinkage and improve electrolyte ab-

†To whom correspondence should be addressed.
E-mail: seongoh@hanyang.ac.kr, huhoon@kitech.re.kr

sorption. PVDF and its copolymer, PVDF-HFP, are the most widely used polymers in the fabrication of electrospinning nonwoven membranes. PVDF-HFP has excellent electrolyte wettability due to its high polarity, low crystallinity, and the presence of C-F groups. It is also a proven electrolyte with relatively high ionic conductivity compared with other polymers. Studies show that PVDF-HFP has a high affinity for liquid electrolyte solutions, which forms a partial gel state. In addition, because PVDF-HFP is generally used as an electrode binder for LIBs, a separator fabricated by PVDF-HFP can reduce interfacial resistance by binding with the electrode [29]. However, in some cases, the use of PVDF or its copolymer as a separator can cause shrinkage and battery safety problems due to poor thermal stability. These problems can be circumvented by using a composite with PAN having high heat resistance at high temperatures [30, 32]. The initial thermal decomposition temperature of PAN is close to 300 °C [40]. This effectively avoids short circuits caused by shrinkage of PE, PVDF, and its copolymer at 150 °C [41,42].

It has been reported that PVDF-HFP nanofibers show poor thermal stability, while having low resistivity and high ionic conductivity. PAN nanofibers, however, show excellent thermal stability, but show low ionic conductivity values according to high resistance values. In this study, we aimed to develop separators having both high thermal stability and good ionic conductivity by manufacturing the PVDF-HFP and PAN bicomponent nanofibers. The PVDF-HFP, PAN and PVDF-HFP/PAN bicomponent nanofibers were fabricated by electrospinning. And the morphologies, crystallinity, shrinkage, tensile strength, thermal stability, wettability, ionic conductivities and electrochemical performances of nanofibers as separators in batteries were investigated and compared with those of PE separator.

EXPERIMENTAL

1. Materials

Pellets of PVDF-HFP (average Mw=400,000; average Mn=130,000; Sigma-Aldrich), PAN (average Mw=150,000; Sigma-Aldrich), N,N-dimethylformamide (DMF, 99.5%, SAMCHUN co. Ltd.), and n-butyl alcohol (99.5%, SAMCHUN) were purchased and used without further purification. A liquid electrolyte, 1.0 M lithium hexafluorophosphate dissolved in ethylene carbonate and ethyl methyl carbonate (EC+EMC 1 : 1 by volume, +FEC 5 wt%, Soulbrain Co. Ltd), a PE separator (Separator 2400), lithium metal (counter electrode), copper foil (24 μm), and a CR2032-type coin cell were purchased from Soulbrain Co., Ltd. Anode materials (Si/C composite) were supplied by Grapsil Co., Ltd.

2. Nanofiber Membrane Preparation by Electrospinning

A 15, 18, 20 wt% of PVDF-HFP and 8, 10 wt% of PAN solution were prepared by dissolving PVDF-HFP pellets and PAN powder in a dimethylformamide (DMF) with magnetic stirring for 8 h at 60 °C. The PVDF-HFP solution was prepared by dissolving 2.25 g, 2.7 g, and 3.0 g of PVDF-HFP pellets in 12.75 g, 12.3 g, and 12 g of DMF solvent under stirring for 8 h at 60 °C. The PAN solution was prepared by dissolving 1.2 g and 1.5 g of PAN in 13.8 g and 13.5 g of DMF under stirring for 8 h at 60 °C. The mixed solution was prepared according to different weight ratios of 18 wt% PVDF-HFP and 10 wt% PAN. The electrospinning process was performed by setting an applied voltage of 11.5 to 16.5 kV (1 mA), an injection speed of 1.5 mL/h, and a tip collector distance of 18 cm. To form a stable Taylor cone of the solution during electrospinning, an experiment was conducted by gradually increasing the voltage from a low applied voltage to a high applied voltage. All nanofiber samples were used after drying at 60 °C for one day.

3. Cell Assembly

Preparation of Si/C anode (working electrode): Si and graphite, conductive additives (SFG), and binders (CMC, SBR) were dissolved in deionized water at a mass ratio of : 5 : 3. Subsequently, the slurry was coated on copper foil (24 μm) using a doctor blade. Si/C anode is dried at 120 °C for at least 12 hours before the fabrication of cells. Anode (14 Ø), Li metal (counter electrode, 16 Ø), and separator (19 Ø) were all punched out with cutters of different sizes. Finally, cell fabrication was carried out in a glove box filled with inert argon gas.

4. Characterization

Scanning electron microscopy (SEM, OXFORD, x-act 6) was employed to investigate the morphology and structure of the electrospun nanofiber-based web. The samples were subjected to platinum sputter-coating in a vacuum prior to imaging. The average fiber diameter (AFD) was determined by measuring the fibers with the ImageJ software at more than 80 places in the SEM images.

The functional group of the nanofiber-based web was also characterized by Fourier transform infrared (FT-IR) spectroscopy (PerkinElmer, Spotlight 200i) in attenuated total reflection mode, and the wavenumber ranged from 650 to 4,000 cm^{-1}.

X-ray diffraction (XRD) patterns of nanofiber webs were analyzed with a Dong-il Shimadzu, XRD-6100 apparatus in a range of 5°-40° at a scan rate of 5° min^{-1}. Thickness analysis of the nanofiber webs involved using a focused ion beam (FIB) (FEI Company, Helios 600i). A differential scanning calorimeter (DSC; PerkinElmer, DSC 8500), thermogravimetric analyzer (TGA; PerkinElmer, Pyris 1) and a shrinkage test were used to evaluate the thermal property and thermal dimensional stability. After exposure to a circular sample 19 mm in diameter at temperatures of 90, 160, 180 and 200 °C for 1 h, the shrinkage rate was calculated using Eq. (1) [28]:

$$\text{Shrinkage}\ (\%) = \left[\left(S_0 - \frac{S_1}{S_0}\right)\right] \times 100 \quad (1)$$

where S_0 and S_1 represent the diameter of the nanofiber-web before and after exposure, respectively.

The mechanical properties of the nanofiber-based web were measured by a KMT, T7000M Universal Testing Machine at a speed of 20 mm/min, and the size of each specimen was cut into 15-45 mm. At least three groups of tests were performed on each sample and an average was recorded. The electrolyte wettability was investigated through an electrolyte absorption test and a contact angle measurement. In the electrolyte uptake test, the weight was measured before and after immersing in the electrolyte for 2 hours. The contact angle was measured after 1 minute. The electrolyte uptake of all samples was calculated by the differential weight method according to Eq. (2) [28]:

$$EU = \frac{W_1 - W_0}{W_0} \times 100 \quad (2)$$

where W_0 and W_1 represent the weights of nanofiber-web before

and after being immersed in the electrolyte, respectively. The porosity of the nanofiber web was determined in the same way as the electrolyte uptake method using n-butanol and calculated by Eq. (3) [28]:

$$P = \frac{W_w - W_d}{\rho \times V} \times 100\% \quad (3)$$

where W_d and W_w are the weights of the nanofiber-web before and after absorption of n-butanol, respectively, ρ is the density of n-butanol (0.8098 g cm^{-3}), and V represents the volume of samples.

5. Electrochemical Characterization

Ionic conductivity can be calculated by Eq. (4):

$$\sigma = \frac{d}{R_b \times S} \quad (4)$$

where d is the thickness of the separator (cm), R_b is the bulk resistance and S is the effective area of the separator (cm^2).

The electrochemical stability window of the nanofiber web-applied cell was measured in linear sweep voltammetry mode (LSV) at a scan rate of 10 mV/s over a potential range of 3.0 to 5.0 V. AC impedance measurements were performed. The potential amplitude was 5 mV and the frequency range was 0.1-10^5 Hz. A battery cycler (WBCS3000S) was used to test the battery cycling from 0.01 to 1.5 V. Cycling performance measurements were performed at 0.5 C after three cycles at 0.1 C for formation, and c-rate performance was measured at various current densities ranging from 0.2 to 3 C for both charge and discharge at 25 °C (each 5 cycles at current density).

RESULTS AND DISCUSSION

1. Morphology and Structure of Nanofiber-based Web

Fig. 1 indicates the surface morphology and average fiber diameter (AFD) of PVDF-HFP, PAN, and PVDF-HFP/PAN nanofibers. Since the nanofiber nonwoven fabric obtained by electrospinning has a high specific surface area, the electrolyte absorption rate may

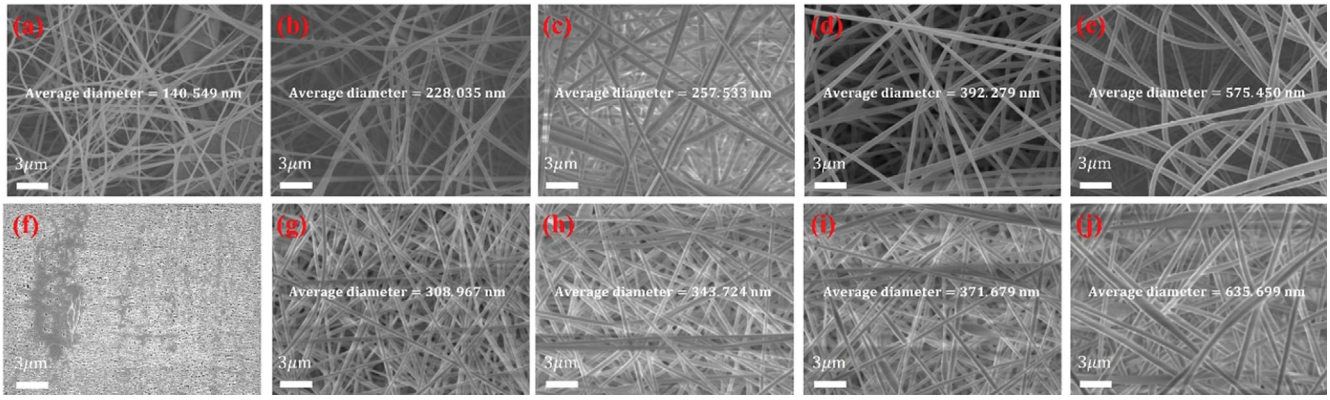

Fig. 1. SEM images of PVDF-HFP 15-20 wt% (a)-(c), PAN 8-10 wt% (d)-(e), PE (f), various ratios of PVDF-HFP/PAN (g)-(j) nanofibers and average diameter.

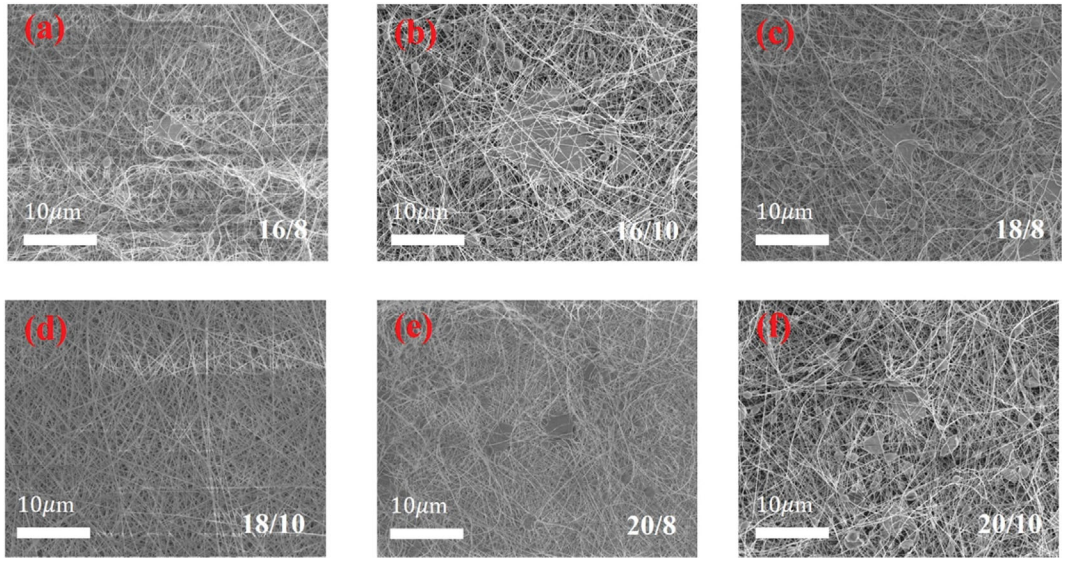

Fig. 2. SEM images of bicomponent nanofibers at various mixing ratios of PVDF-HFP/PAN: (a) 16/8, (b) 16/10, (c) 18/8, (d) 18/10, (e) 20/8, and (f) 20/10.

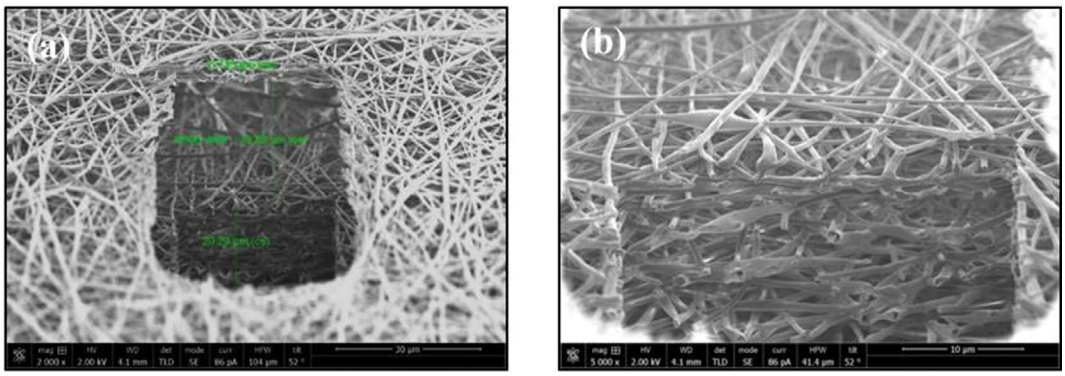

Fig. 3. FIB image of electrospinning nanofiber web cross-section and thickness.

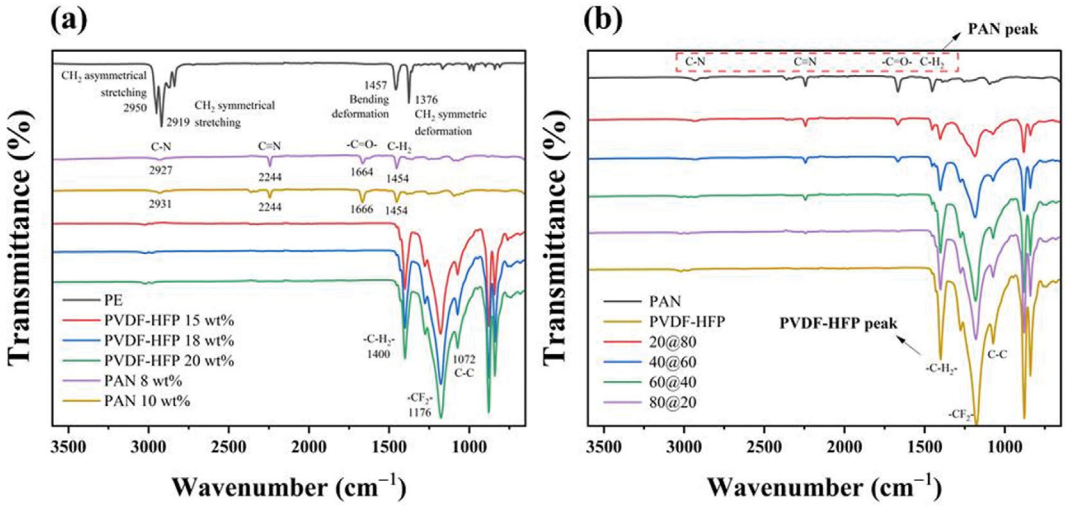

Fig. 4. FT-IR spectra of PE, PVDF-HFP, PAN (a) and PVDF-HFP/PAN (b) nanofibers.

be high. Electrolytes are considered the main medium of ion transfer in LIBs. AFD tends to increase as the concentration of the precursor solution increases. The AFD of PVDF-HFP is 140.549, 228.035, and 257.533 nm, and the AFD of PAN is 392.279, 575.450 nm. In general, the thickness of the fiber tends to increase as the concentration of the solution increases [42]. The PVDF-HFP nanofibers manufactured with 16, 18, and 20 wt% solutions showed an increase in bead and swelling shape at low concentration, and a thicker fiber thickness at high concentration (Fig. 1(a)-(c)). The nanofibers manufactured with 8 and 10 wt% of PAN solution showed a fiber form without beads and swelling, but its thickness increased as the concentration increased (Fig. 1(d)-(e)).

To select the appropriate concentration of PVDF-HFP and PAN bicomponent through electrospinning, the surface morphology of fabricated nanofiber was observed (Fig. 2). Fig. 2(a)-(f) shows the fiber images for each concentration of the mixed solution of PVDF-HFP and PAN. Among them, bead and swelling shapes were observed in all samples except for the nanofibers made by mixing 18 wt% of PVDF-HFP and 10 wt% of PAN. Through these SEM images, the concentration of the PVDF-HFP and PAN mixture without beads and swelling was selected. In addition, four different ratios of nanofibers were fabricated and thermal, mechanical, wettability and electrochemical analyzes were conducted.

The thickness of the manufactured fiber was measured through FIB (Fig. 3). The thickness of the nanofibers that did not go through the press process was about 53 μm, including the empty space, and the fibers were layered.

FT-IR analysis was performed to check the characteristic peaks of PE, PVDF-HFP, PAN and PVDF-HFP/PAN (Fig. 4). Peaks of PVDF-HFP fibers were found in 1,072, 1,176 and 1,400 cm^{-1}. Each peak corresponds to vibration in C-C, C-F_2 and C-H_2. The peak of the PAN fiber was found in 1,452, 1,664, 2,244 and 2,927 cm^{-1}. Each peak corresponds to C-H_2, C=O, C≡N and C-N vibration. The FT-IR result of the PVDF-HFP/PAN fiber indicates that there is no change in the chemical structure of the two solutions. As the mixing ratio increases in each material, the intensity of the characteristic peak increases.

The XRD analysis was performed to view the crystallinity of the polyolefin separator and the nanofiber separator. The polyolefin separator showed three strong peaks at 2θ=14.10°, 17.2° and 18.60°, and PVDF-HFP and PANs showed peaks at 2θ=20.5° and 2θ=17.2° (Fig. 5). Bicomponent nanofibers made at different ratios show both the characteristic peaks of PVDF-HFP and PAN. The polyolefin separator shows a relatively high crystal compared to the

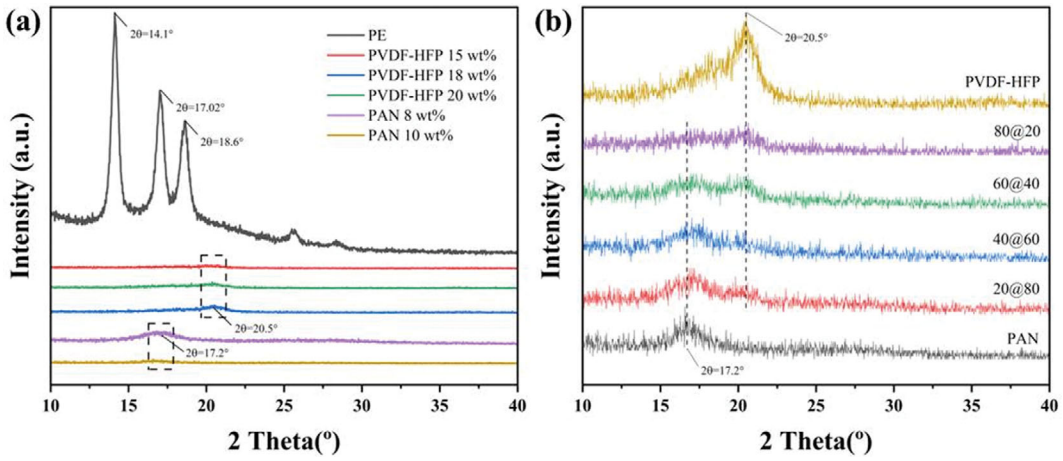

Fig. 5. XRD spectra of PE, PVDF-HFP, PAN (a) and PVDF-HFP/PAN (b) nanofibers.

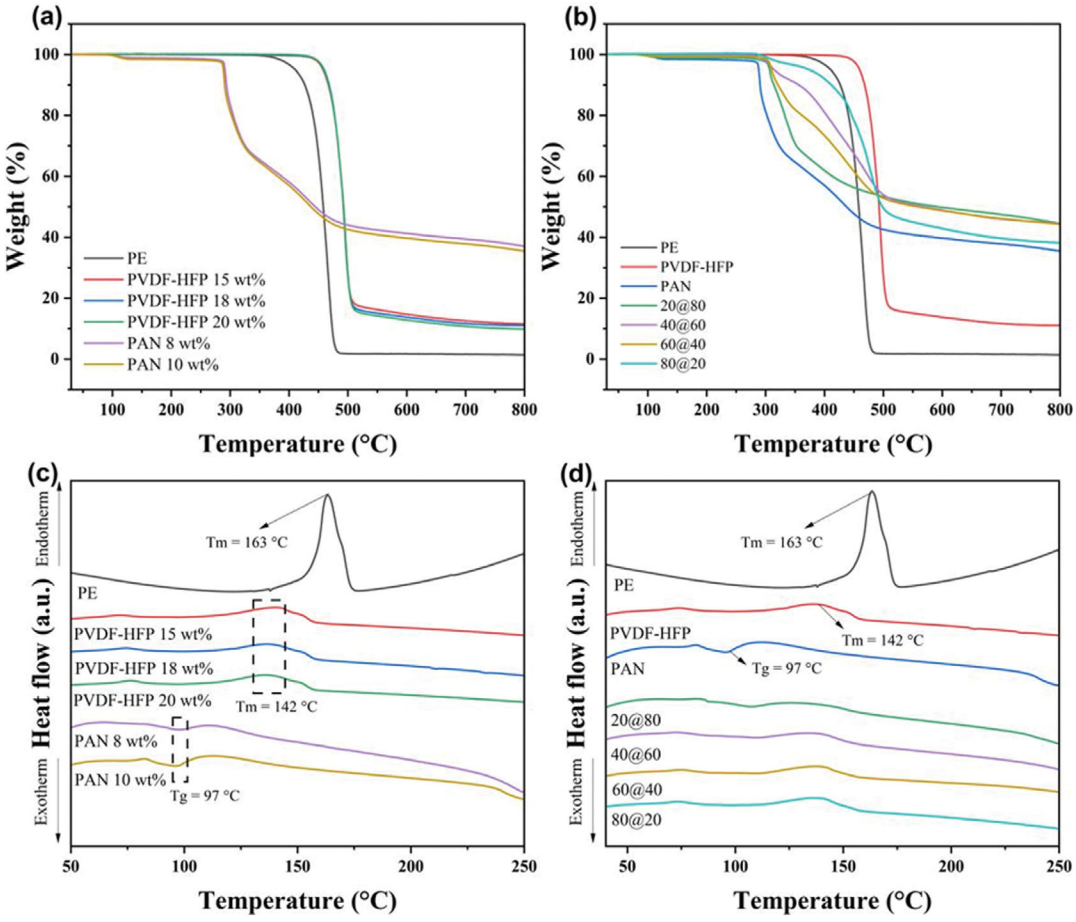

Fig. 6. Thermogravimetric analysis (a)-(b) and Differential scanning calorimetry (c)-(d) of PE, PVDF-HFP, PAN and PVDF-HFP/PAN nanofibers.

nanofiber web. Among the battery membrane requirements, excellent electrolyte absorption is an important factor in determining the electrochemical performance of the battery. Crystallinity inhibits the reduction of electrolyte absorption and the mobility of lithium ions. The polyolefin separator has high crystallinity, so it has low cycle stability, c-rate performance and discharge capacity retention.

2. Thermal Stability Characterizations

TGA, DSC, and shrinkage tests were performed to investigate the thermal properties of the separator. TGA analysis was performed from room temperature to 800 °C, and DSC was performed between room temperature and 250 °C. In both analyses, the heating rate was 10 °C/min. PE and PVDF-HFP are low in weight at the final

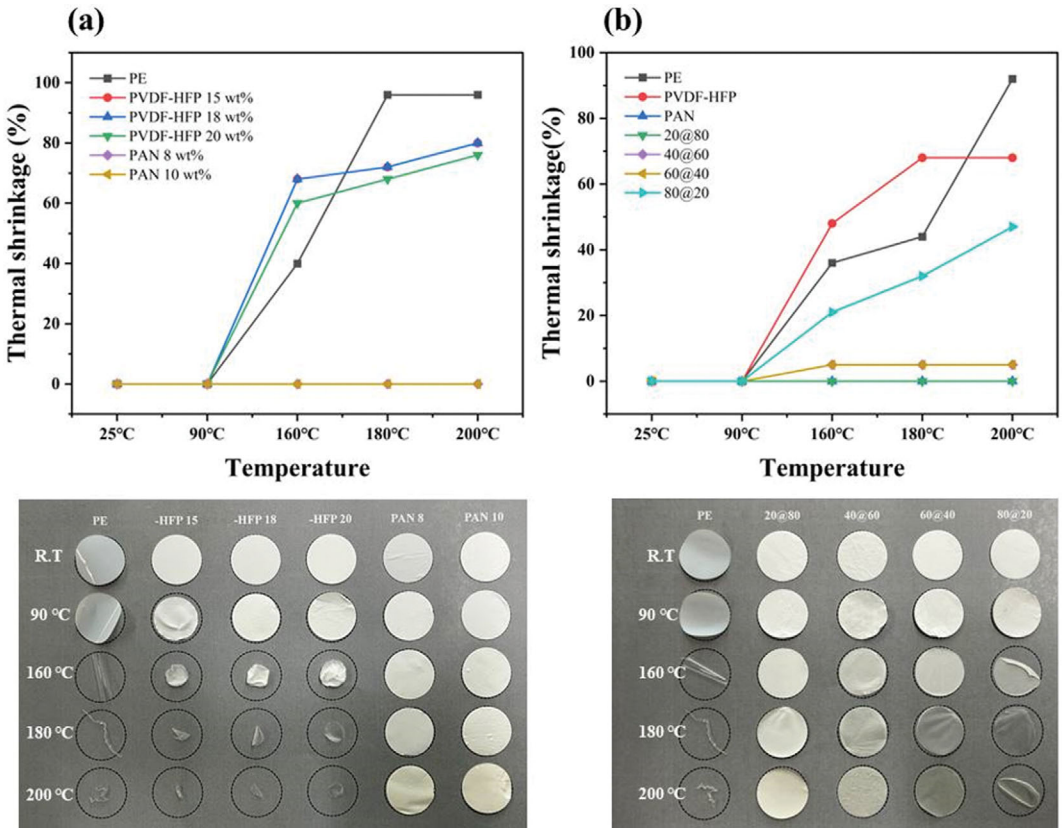

Fig. 7. Thermal shrinkage test of PE, PVDF-HFP (a), PVDF-HFP/PAN bicomponent (b) and test images.

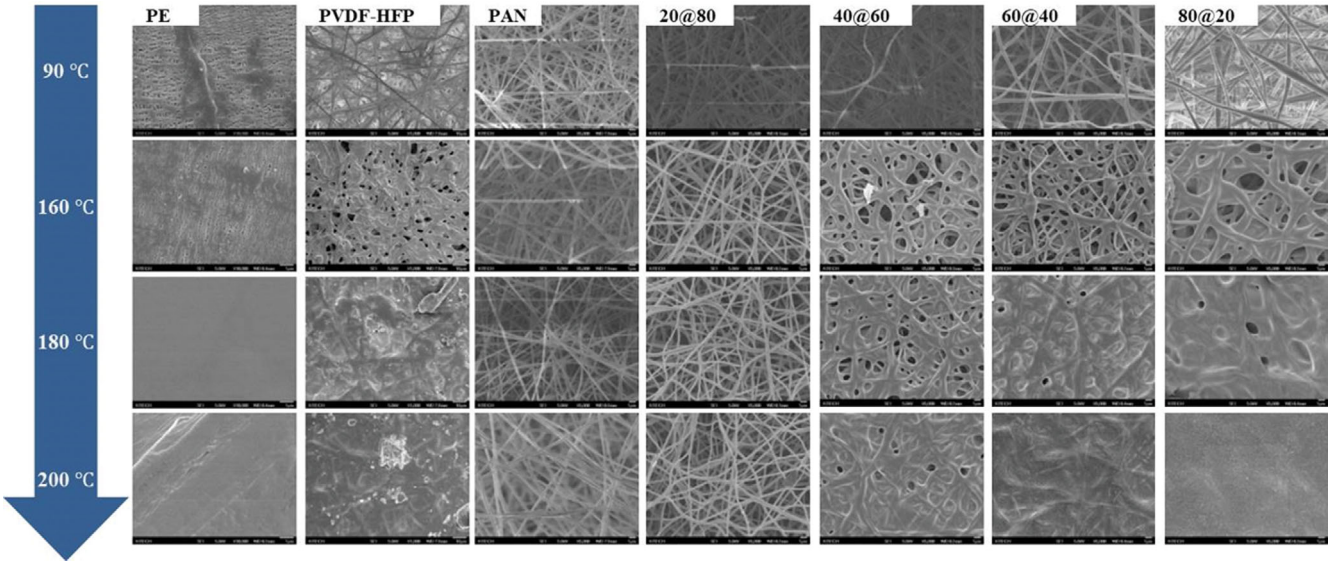

Fig. 8. Thermal shrinkage SEM image of PE, PVDF-HFP, PVDF-HFP/PAN bicomponent nanofibers.

temperature due to rapid weight loss as the temperature increases. However, PAN decomposes at relatively low temperatures and has a high weight percentage at the final temperature due to small weight reduction. The decomposition temperatures of PE, PVDF-HFP, and PAN are 400, 450, and 300 °C, respectively. PE and PVDF-HFP decompose at higher temperatures than PAN but are difficult to use alone. Because PE and PVDF-HFP have low T_m values, they melt when exposed to high temperature environments (Fig. 8). As mentioned above, PE and PVDF-HFP have a T_m of 163 °C and 142 °C (Fig. 6(c)). Therefore, both show high shrinkage at 160, 180, and 200 °C (Fig. 7(a)). PAN decomposes at lower temperatures than PE and PVDF-HFP, but T_m values did not appear within the DSC analy-

Table 1. PVDF-HFP, PAN precursor solution properties and electrospinning conditions

Fiber morphology	Composition	Temp (°C) & Humidity (%)	Voltage (kV)	Average diamether (nm)
NFs	PVDF-HFP 15 wt%	13.0 & 28	15.5	140.549
NFs	PVDF-HFP 18 wt%	11.4 & 28	14.0	228.035
NFs	PVDF-HFP 20 wt%	10.8 & 28	11.5	257.533
NFs	PAN 8 wt%	16.9 & 26	16.5	392.279
NFs	PAN 10 wt%	14.2 & 26	16.0	575.450

Table 2. PVDF-HFP@PAN bicomponent precursor solution properties and electrospinning conditions

Fiber morphology	Composition	Temp (°C) & Humidity (%)	Voltage (kV)	Average diamether (nm)
NFs	(20)PVDF-HFP (80)PAN/20@80	14.3 & 26	15.5	308.967
NFs	(40)PVDF-HFP (60)PAN/40@60	18.7 & 24	15.0	369.660
NFs	(60)PVDF-HFP (40)PAN/60@40	16.8 & 24	14.3	353.676
NFs	(80)PVDF-HFP (20)PAN/80@20	19.2 & 24	13.0	635.699

Table 3. Tensile strength, Young's module, porosity, electrolyte uptake, contact angle of PE and as-prepared PVDF-HFP, PAN nanofibers

Samples	Tensile strength (N/mm^2)	Porosity (%)	Electrolyte uptake (%)	Contact angle (°)
PE	12.85	40.00	116	33.17
PVDF-HFP 15 wt%	4.75	69.57	876	<1
PVDF-HFP 18 wt%	7.83	62.91	816	<1
PVDF-HFP 20 wt%	6.10	66.76	852	<1
PAN 8 wt%	0.27	75.59	2,681	<1
PAN 10 wt%	1.72	71.50	2,217	<1

Table 4. Tensile strength, Young's module, porosity, electrolyte uptake, contact angle of PE and as-prepared PVDF-HFP/PAN nanofibers at various mixing ratios

Samples	Tensile strength (N/mm^2)	Porosity (%)	Electrolyte uptake (%)	Contact angle (°)
PE	12.847	40.00	116	33.17
20@80	1.371	76.49	1,299	<1
40@60	1.945	72.51	1,222	<1
60@40	2.635	66.41	1,142	<1
80@20	2.912	62.77	774	<1

sis temperature range. This result may maintain the separator shape at higher temperature environment than PE and PVDF-HFP when applied to the battery separator. The excellent thermal properties of PAN also appear in binary PVDF-HFP/PAN nanofibers. All nanofibers with PAN content exceeding 40% show a shrinkage rate of less than 5% at 200 °C (Fig. 7(b)). The low thermal properties of conventionally used polyolefin separators were confirmed through TGA, DSC and shrinkage test. When PAN with high thermal stability was used as a blend material, rapid weight loss and shrinkage were reduced.

3. Mechanical Properties and Wettability Analysis

The mechanical properties of the separator are one of the major factors in batteries. The separator physically separates the cathode and the anode and prevents an electrical short circuit of the cell induced from the growth of lithium dendrite. To prevent such an electrical short circuit, the separator should not be penetrated due to lithium dendrite while the cell is being driven. A polyolefin separator in the form of a film has an excellent tensile strength value (12.847 N/mm^2). However, nanofiber separators manufactured through electrospinning have relatively low tensile strength values

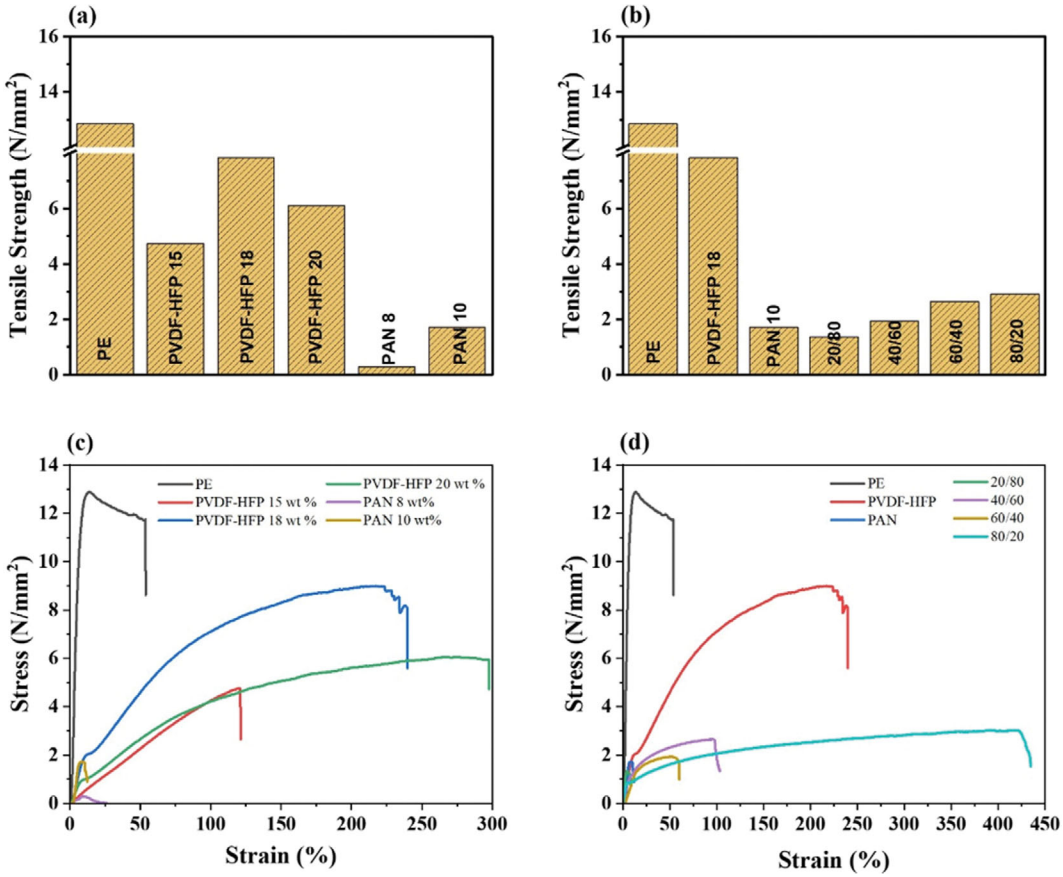

Fig. 9. UTM data (a), (b) and S-S Curve (c), (d) of PE, PVDF-HFP, PAN and PVDF-HFP/PAN bicomponent nanofibers.

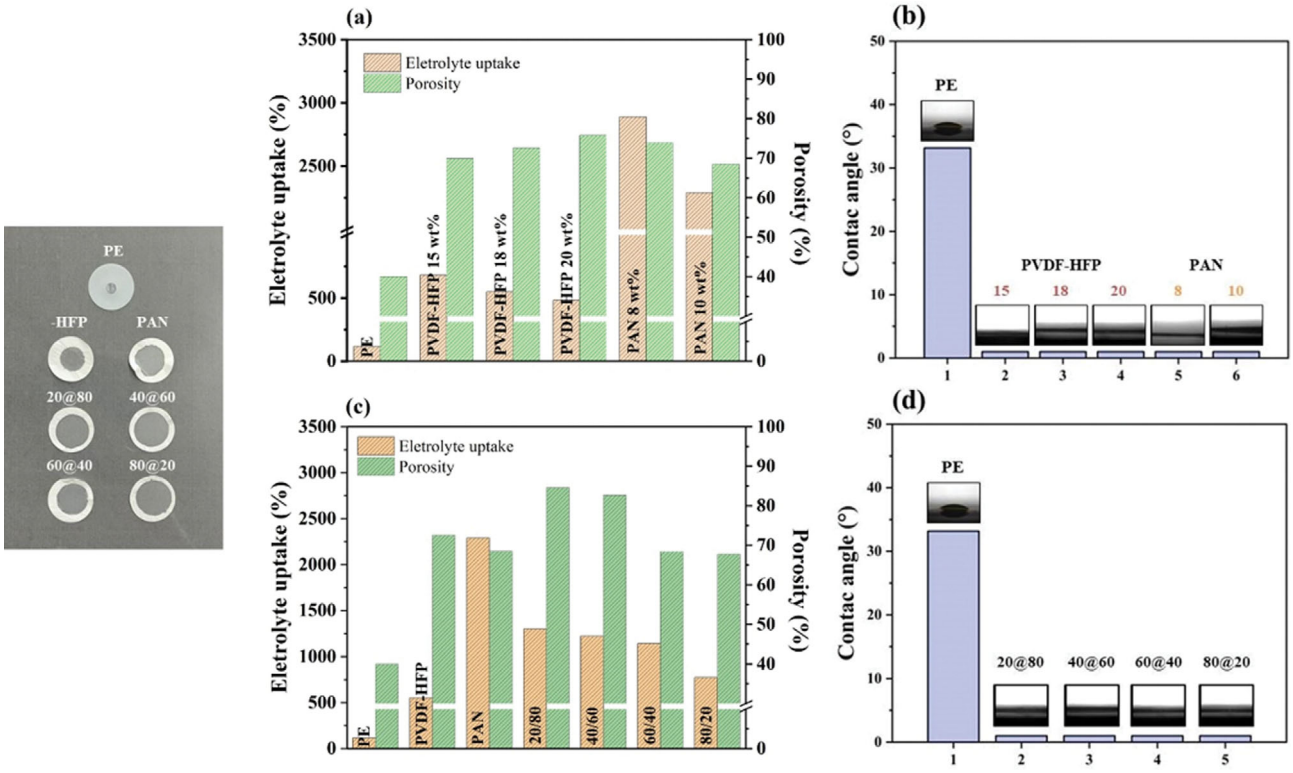

Fig. 10. Wettability uptake, porosity (a), (c) and contact angle test (b), (d) of PE, PVDF-HFP, PAN and PVDF-HFP/PAN nanofibers.

due to their high porosity. The tensile strength and young's module values of PE, PVDF-HFP, and PAN are shown in Table 3 and Fig. 9.

PVDF-HFP (7.831 N/mm^2) has the highest tensile strength value at 18 wt%, and PAN (1.718 N/mm^2) has a high tensile strength value at 10 wt%. The nanofiber separator tends to have a higher tensile strength value as the porosity decreases. The high porosity of nanofiber mats is difficult to withstand the force applied from the outside. As the PVDF-HFP ratio increases, the tensile strength value of the bicomponent nanofiber increases and the porosity tends to decrease. The bicomponent PVDF-HFP/PAN nanofibers compensate for the disadvantages of each material. The PAN lowers the shrinkage rate of the separator in terms of thermal stability, and the PVDF-HFP increases the tensile strength value.

The wettability of a membrane is characterized by absorption, porosity, and contact angle of the membrane and electrolyte. As shown in Fig. 9(a), the electrolyte wettability is 116, 816 and 2,217% for PE, PVDF-HFP and PAN membranes, respectively. The nanofiber membrane having a three-dimensional structure has an excellent wettability to an electrolyte solution. The electrolyte, porosity and contact angle values of the different membranes are presented in Table 3. The nanofiber membrane absorbs more electrolyte due to its high mobility. In addition, since PVDF-HFP has a polar C-F bond, it has excellent interactions with electrolytes made of organic solvents. The contact angle between PE and the nanofiber membrane is 33.17° and less than 1°. Polyolefin separators have low porosity and low organic electrolyte absorption due to their high crystallinity and non-polarity. However, nanofibers have high porosity, electrolyte uptake and lower contact angle.

4. Electrochemical Characterization

The range of the electrochemical window reflects the electrochemical stability of the separator. The LSV curves of the polyolefin membrane and the nanofiber membrane were tested by the LSV method (Figs. 11 and 12). In the LSV curve, there is no polarization and no electrochemical reaction at the low voltage section. To be used at high voltage batteries, the oxidation reaction of the electrodes should be small within a wide electrochemical window range. However, when the PVDF-HFP and PAN membrane are used alone in a cell, the current change is higher between 4-5 V than the polyolefin separator. Thus, using pure PVDF-HFP and PAN nanofibers in the high voltage range has less stability of the electrode than using a polyolefin separator. Cells using PVDF-HFP/PAN nanofibers show different result values. Cells using the polyolefin separator have a larger current value from 4 V, while PVDF-HFP/PAN separator has a larger current value between 4.2 and 4.25 V. That is, PVDF-HFP/PAN nanofibers are more suitable for use in batteries requiring high voltage than pure PVDF-HFP and PAN.

Since the PVDF-HFP nanofibers have a lower resistance than PE and PAN, the discharge capacity value is large. However, capacity reduction begins to increase after 50 cycles to proceed with a long cycle. However, PAN nanofibers have a discharge capacity value smaller than PVDF-HFP, but as the cycle progresses, the slope of capacity reduction is constant. PVDF-HFP and PAN have different advantages and disadvantages in electrochemical performance. Bicomponent nanofibers complement the disadvantages of low discharge capacity and long-term cycle stability of each of the two materials. Fig. 12(c)-(d) shows the cycle performance of bicomponent nanofibers. As the PVDF-HFP ratio increases, the initial cycle discharge capacity value increases, but the long-term cycle stability decreases. The 80/20 sample showed a significant decrease in dis-

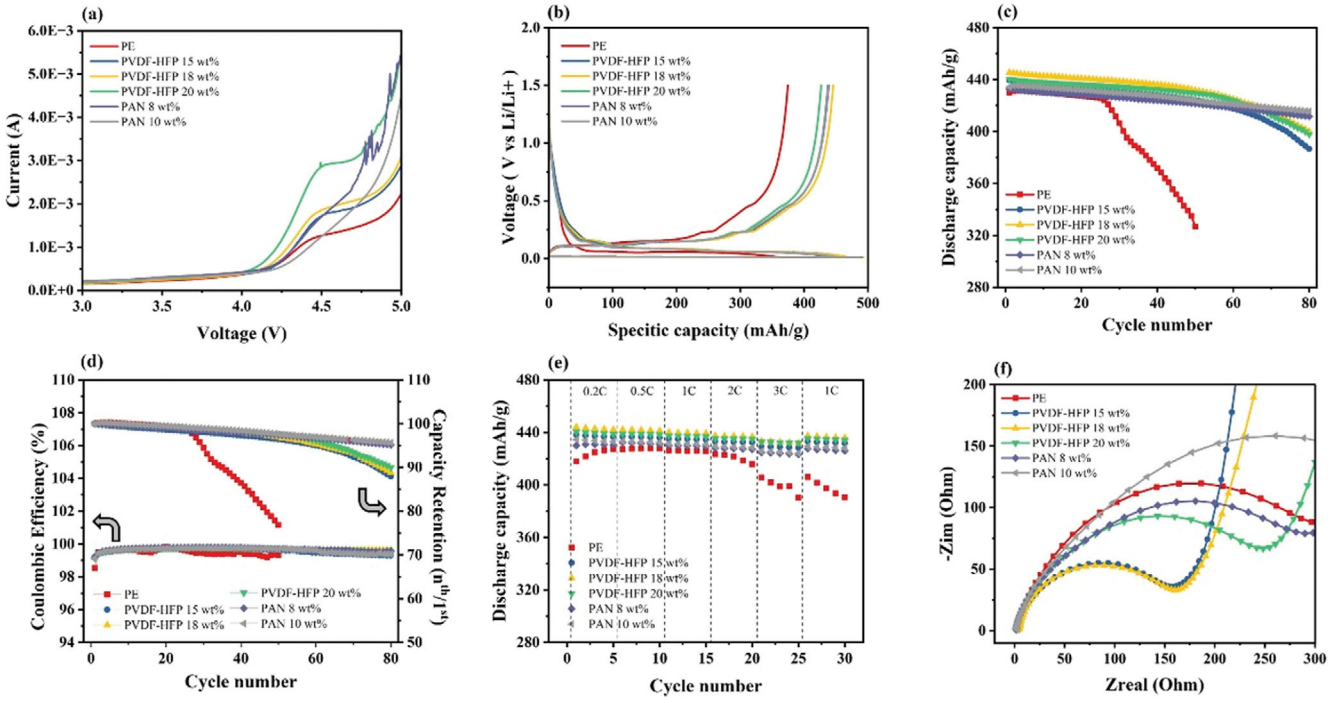

Fig. 11. Electrochemical analysis of PE, PVDF-HFP, PAN; (a) LSV curve, (b) First cycle efficiency, (c) Cycle performance, (d) Coulombic Efficiency and Capacity Retention, (e) C-rate performance, (f) Electrochemical impedance spectroscopy.

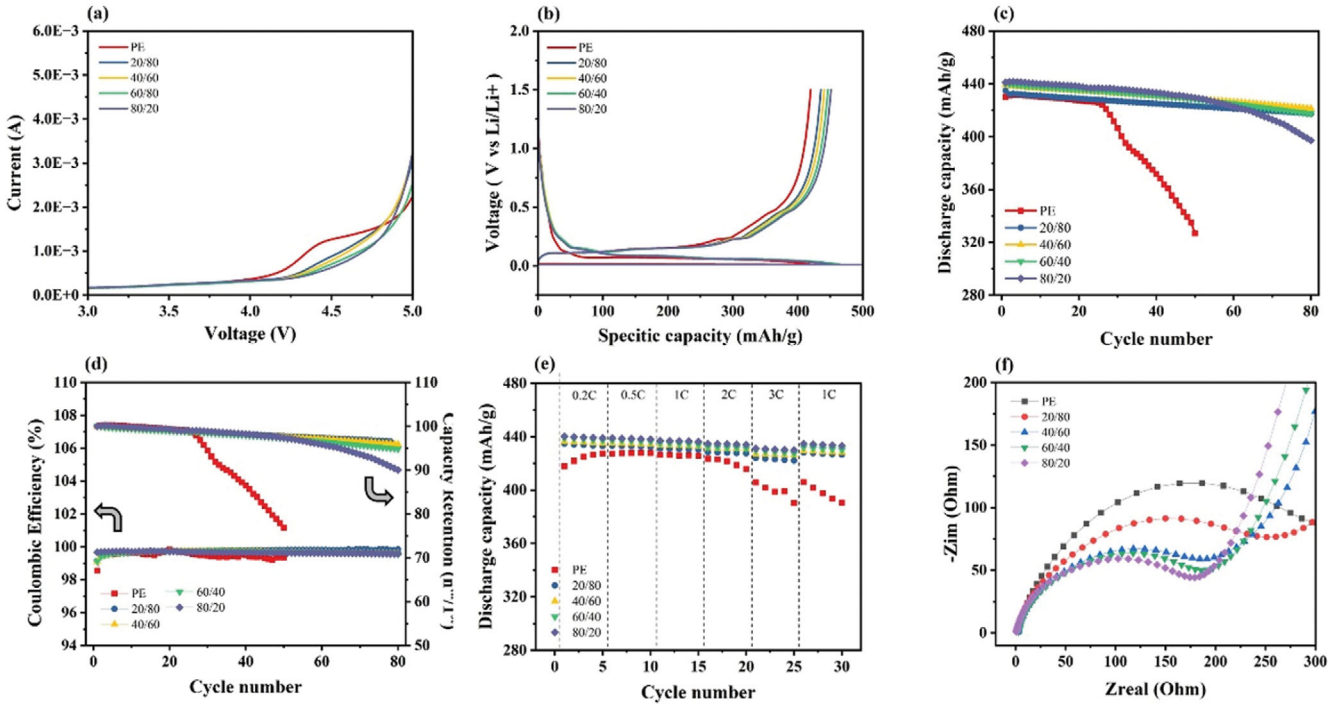

Fig. 12. Electrochemical analysis of PE, PVDF-HFP/PAN bicomponent nanofiber; (a) LSV curve, (b) First cycle efficiency, (c) Cycle performance, (d) Coulombic Efficiency and Capacity Retention, (e) C-rate performance, (f) Electrochemical impedance spectroscopy.

charge capacity and capacity retention rate like pure PVDF-HFP. Bicomponent nanofibers having a high PAN ratio (>40 wt%) have a relatively low discharge capacity, but their discharge capacity and capacity retention are constantly reduced in terms of a long-term cycle.

Fig. 12(e) shows the discharge capacity values according to the change in C-rate. Cells using polyolefin separators have more initial unexpressed capacity values than nanofiber separators, and capacity recovery after high c-rate operation is not carried out properly. The bicomponent nanofibers have a relatively high discharge capacity value even at high c-rate of charging/discharging, and capacity recovery is carried out even after high c-rate processes.

Fig. 11(f) shows the Nyquist plot for the measurement of PE, PVDF-HFP, and PAN ionic conductivity in the cell. The ionic con-

Table 5. Thickness, bulk resistance and ionic conductivity of PE separator and as-prepared PVDF-HFP, PAN nanofibers

Samples	Thickness (μm)	Bulk resistance (Ω)	Ionic conductivity ($mS \cdot cm^{-1}$)
PE	25	1.17	1.39
PVDF-HFP 15 wt%	46	0.81	3.68
PVDF-HFP 18 wt%	51	0.86	3.86
PVDF-HFP 20 wt%	54	0.95	3.69
PAN 8 wt%	50	1.09	2.98
PAN 10 wt%	52	1.12	3.01

Table 6. Thickness, bulk resistance and ionic conductivity of PE separator and as-prepared PVDF-HFP/PAN nanofibers at various mixing ratios

Samples	Thickness (μm)	Bulk resistance (Ω)	Ionic conductivity ($mS \cdot cm^{-1}$)
PE	25	1.17	1.39
20@80	51	1.09	3.06
40@60	49	1.02	3.24
60@40	50	0.96	3.38
80@20	49	0.91	3.50

ductivity according to the bulk resistance (R_b) obtained from the plot was calculated through Eq. (4) and shown in Table 5. The ionic conductivity values of the cells using PVDF-HFP/PAN were also calculated in the same way and shown in Table 6. The maximum ion conductivity of PVDF-HFP, PAN and PVDF-HFP/PAN at room temperature is 3.86, 3.01, and 3.50 mS/cm^{-3}. These values are sufficient for practical LIBs compared to PE. The high ionic conductivity comes mainly from large amounts of liquid electrolytes embedded in pore networks of nanofiber-based separators. As mentioned above, a structure with three dimensions and high porosity can contain a large amount of electrolytes. The amorphous HFP copolymer region also absorbs liquid electrolytes and the crystalline PVDF region promotes ionization of lithium salts, increasing the concentration of Li+ ions, thereby improving lithium ionic conductivity [43]. The three-dimensional structure and pore network of the nanofiber-based separator increase ionic conductivity because it wets a large amount of liquid electrolyte. In addition, the HFP copolymer region absorbs a liquid electrolyte into an amorphous region, and the crystalline PVDF region promotes ionization of lithium salts. Thus, the lithium-ion conductivity is enhanced by increasing the Li ion concentration.

In this study, PVDF, PAN, and PVDF-HFP/PAN nanofibers were fabricated using electrospinning. Nanofiber-based separators absorb numerous electrolytes due to their three-dimensional structure and high porosity. Therefore, LIB cells manufactured with nanofibers for separators generally have superior electrochemical values compared with polyolefin separators. But the electrochemical performance of cells at high temperatures around 140 °C is needed for the practical applications of this study [44].

CONCLUSIONS

We intend to compensate for the shortcomings of the existing polyolefin separator by applying a nanofiber separator to LIB. PVDF-HFP is composed of an amorphous HFP copolymer region and a crystalline PVDF region. The amorphous region absorbs the electrolyte, and the crystalline region promotes ionization of the lithium salt, thereby increasing the concentration of lithium ions. The characteristics of such PVDF-HFP contribute to high ionic conductivity (3.50 mS/cm^{-3}) at room temperature. A PAN having high thermal characteristics maintains a 3D structure at high temperature environment, thereby preventing physical contact between the cathode and anodes caused by separator contraction. PVDF-HFP and PAN show different characteristics in cycle performance. PVDF-HFP with high ionic conductivity has excellent discharge capacity, but it shows a rapid decrease capacity reduction. PAN shows less capacity reduction but a relatively low discharge capacity. The bicomponent nanofiber separator has all the advantages of each material. Based on electrochemical results, PVDF-HFP/PAN nanofibers have a high ionic conductivity and long-term cycle stability at room temperature.

ACKNOWLEDGEMENTS

This work was supported by the Graduate School of Post Plastic specialization of Korea Environmental Industry & Technology Institute grant funded by Ministry of Environment, Republic of Korea.

REFERENCES

1. B. Scrosati and J. Garche, *J. Power Sources*, **195**(9), 2419 (2010).
2. J. Goodenough and K. S. Park, *J. Am. Chem. Soc.*, **135**(4), 1167 (2013).
3. M. Yang and H. Junbo, *Membranes*, **2**(3), 367 (2012).
4. J. Tarascon and A. Michel, *Nature*, **414**, 359 (2001).
5. J. Hassoun, *Adv. Mater.*, **21**(47), 4807 (2009).
6. S. Megahed and S. Bruno, *J. Power Sources*, **51**(1-2), 79 (1994).
7. J. Choi, *Nanoscale*, **5**(8), 3230 (2013).
8. J. B. Goodenough and K. Youngsik, *Chem. Mater.*, **22**(3), 587 (2010).
9. F. Gao, *Int. J. Electrochem. Sci.*, **15**, 1391 (2020).
10. J. Choi and J. K. Patrick, *Curr. Opin. Electrochem.*, **31**, 100858 (2022).
11. M. F. Lagadec, Z. Raphael and W. Vanessa, *Nature Energy*, **4**(1), 16 (2019).
12. G. Venugopal, *J. Power Sources*, **77**(1), 34 (1999).
13. S. S. Zhang, *J. Power Sources*, **164**(1), 351 (2007).
14. X. Huang, *J. Solid State Electrochem.*, **15**(4), 649 (2011).
15. W. Yi, *J. Power Sources*, **189**(1), 616 (2009).
16. P. Kritzer, *J. Power Sources*, **161**(2), 1335 (2006).
17. J. Miao, *J. Nanosci. Nanotechnol.*, **10**(9), 5507 (2010).
18. W. Chen, *J. Power Sources*, **273**, 1127 (2015).
19. H. Zhao, *Mater. Lett.*, **236**, 101 (2019).
20. D. Wu, *Electrochim. Acta*, **176**, 727 (2015).
21. Y. Zhai, *J. Mater. Chem. A*, **2**(35), 14511 (2014).
22. Z. Liu, *Macromol. Mater. Eng.*, **298**(7), 806 (2013).
23. L. Wang, *Electrochem. Acta*, **300**, 263 (2019).
24. M. Cai, *Nanomaterials*, **9**(1), 39 (2018).
25. M. Cai, *Polymers*, **11**(1), 185 (2019).
26. J. C. Barbosa, *Membranes*, **8**(3), 45 (2018).
27. S. Yang, *RSC Adv.*, **8**(41), 23390 (2018).
28. M. Cai, *J. Power Sources*, **461**, 228123 (2020).
29. T. Evans, *J. Power Sources*, **292**, 1 (2015).
30. D. J. Liaw, *Prog. Polym. Sci.*, **37**(7), 907 (2012).
31. L. Wang, *Compos. Commun.*, **16**, 150 (2019).
32. J. Hao, *J. Membr. Scie.*, **428**, 11 (2013).
33. J. Ding, *J. Electrochem. Soc.*, **159**(9), A1474 (2012).
34. Z. Zhong, *Mater. Sci. Eng.: B*, **177**(1), 86 (2012).
35. Z. Zhong, *Ionic*, **18**(1), 47 (2012).
36. O. Fu, *Energy Technol.*, **6**(1), 144 (2018).
37. T. H. Q. Zhang and S. Kuangzheng, *Mater. Lett.*, **245**, 10 (2019).
38. H. Liu, *J. Solid State Electrochem.*, **22**(11), 3579 (2018).
39. Z. Y. Z. Liang and L. Yanxi, *Energies*, **12**(17), 3391 (2019).
40. J. Zhao, *Coatings*, **8**(12), 437 (2018).
41. J. Zhang, *Sci. Rep.*, **4**(1), 1 (2014).
42. X. Huang and H. Jonathon, *J. Membr. Sci.*, **425**, 163 (2013).
43. Y. Baskakova and O. Yarmolenko, *Russ. Chem. Rev.*, **81**, 367 (2012).
44. J. Oh, H. Jo, H. Lee, H. K. Kim, Y. M. Lee and M. H. Ryou, *J. Power Sources*, **430**, 130 (2019).